



Cite this: *J. Mater. Chem. C*, 2020, **8**, 5732

## Phonons and excitons in $\text{ZrSe}_2\text{--ZrS}_2$ alloys†

Sean M. Oliver,<sup>ab</sup> Joshua J. Fox,<sup>cd</sup> Arsalan Hashemi,<sup>e</sup> Akshay Singh,<sup>id fg</sup> Randal L. Cavallero,<sup>cd</sup> Sam Yee,<sup>ab</sup> David W. Snyder,<sup>cd</sup> R. Jaramillo,<sup>id f</sup> Hannu-Pekka Komsa<sup>id eh</sup> and Patrick M. Vora<sup>id \*ab</sup>

Zirconium disulfide ( $\text{ZrS}_2$ ) and zirconium diselenide ( $\text{ZrSe}_2$ ) are promising materials for future optoelectronics due to indirect band gaps in the visible and near-infrared (NIR) spectral regions. Alloying these materials to produce  $\text{ZrS}_x\text{Se}_{2-x}$  ( $x = 0 \dots 2$ ) would provide continuous control over key optical and electronic parameters required for device engineering. Here, we present a comprehensive analysis of the phonons and excitons in  $\text{ZrS}_x\text{Se}_{2-x}$  using low-temperature Raman spectroscopy and room-temperature spectroscopic ellipsometry (SE) measurements. We extract the Raman-active vibrational mode frequencies and find that they compare favorably with density functional theory (DFT) calculations. Our simulations and polarization-resolved measurements demonstrate that substitutional doping renders infrared (IR) modes to be Raman-active. This leads to a Raman spectrum dominated by nominally IR phonons, a phenomenon that originates from the large ionicity of the  $\text{ZrS}_x\text{Se}_{2-x}$  bonds. SE measurements of the complex refractive index quantify the blue-shift of direct, allowed exciton transitions with increasing S content, and we find strong light–matter interactions with low optical loss in the NIR. Correlating these data with DFT allows for an estimation of the  $\Gamma$ -point exciton binding energy at room temperature. This study illustrates the large effects of alloying on  $\text{ZrS}_x\text{Se}_{2-x}$  and lays the foundation for future applications of this material.

Received 12th February 2020,  
Accepted 17th March 2020

DOI: 10.1039/d0tc00731e

rsc.li/materials-c

## 1 Introduction

The sizable band gaps of monolayer semiconducting transition metal dichalcogenides (TMDs) offer a functional platform for the development of atomically-thin electronics.<sup>1,2</sup> Zirconium disulfide ( $\text{ZrS}_2$ ), for example, has been investigated for optoelectronic applications<sup>3–5</sup> as its 1.7–1.8 eV indirect band gap in the bulk matches well with the upper-edge of the visible spectrum.<sup>5,6</sup> Additionally, recent theoretical predictions have demonstrated that application of compressive and tensile strain to  $\text{ZrS}_2$  provides the opportunity to modify its band gap from 0–2.47 eV, while >8% uniaxial strain is expected to induce an indirect-to-direct band gap transition.<sup>7–10</sup> Such

properties make  $\text{ZrS}_2$  an attractive material for use as the active element in advanced photodetectors and photovoltaics.

The properties of  $\text{ZrS}_2$  may be further enhanced for optoelectronic applications through alloy engineering. This process has been shown to provide a means for the continuous control of band gaps, work functions, lattice constants, and crystal structures.<sup>11,12</sup> For example, recent studies have demonstrated broadband photodetection for visible light in  $\text{ZrS}_2$ -based photodetectors, but their responsivity was found to decrease for infrared (IR) wavelengths.<sup>5,13</sup> The photoresponsivity of  $\text{ZrS}_2$  can be extended into the IR by alloying with the TMD zirconium diselenide ( $\text{ZrSe}_2$ ),<sup>6</sup> a semiconductor with an indirect band gap of 1.07 eV,<sup>14</sup> to produce  $\text{ZrS}_x\text{Se}_{2-x}$  ( $x = 0 \dots 2$ ). Additionally, due to the difference in the Zr–S and Zr–Se bond lengths of  $\text{ZrS}_2$  and  $\text{ZrSe}_2$  that were previously calculated to be 2.57 Å and 2.71 Å,<sup>15</sup> respectively,  $\text{ZrS}_x\text{Se}_{2-x}$  alloys should host an intrinsic lattice strain<sup>16</sup> that may yield a more modifiable band gap. While these characteristics make the  $\text{ZrS}_x\text{Se}_{2-x}$  alloy system of interest for high-performance optoelectronic applications, previous investigations are limited and primarily focus on growth,<sup>17–19</sup> theoretical calculations of electronic and thermoelectric properties,<sup>20–22</sup> angle-resolved photoemission spectroscopy measurements,<sup>23,24</sup> and absorption measurements.<sup>6,25</sup> There are, however, no existing studies of the alloy-dependence of basic material properties such as the phonon mode energies and exciton states.

<sup>a</sup> Department of Physics and Astronomy, George Mason University, Fairfax, VA, USA.  
E-mail: pvora@gmu.edu

<sup>b</sup> Quantum Materials Center, George Mason University, Fairfax, VA, USA

<sup>c</sup> Electronic Materials and Devices Department, Applied Research Laboratory, Pennsylvania State University, University Park, Pennsylvania, USA

<sup>d</sup> 2-Dimensional Crystal Consortium, Materials Research Institute, Pennsylvania State University, University Park, Pennsylvania, USA

<sup>e</sup> Department of Applied Physics, Aalto University, Aalto, Finland

<sup>f</sup> Department of Materials Science and Engineering, Massachusetts Institute of Technology, Cambridge, MA, USA

<sup>g</sup> Department of Physics, Indian Institute of Science, Bangalore, India

<sup>h</sup> Microelectronics Research Unit, University of Oulu, Oulu, Finland

† Electronic supplementary information (ESI) available. See DOI: 10.1039/d0tc00731e

Here, we investigate the effects of alloying on the phonons and excitons in the  $\text{ZrS}_x\text{Se}_{2-x}$  system using low-temperature Raman spectroscopy and room-temperature spectroscopic ellipsometry (SE) measurements. Our interpretation of this data is guided by density functional theory (DFT) calculations of phonon band structures and alloy-dependent mixing energies, lattice constants, and band gaps. Vibrational mode symmetries are assigned to phonons observed in the endpoint compounds  $\text{ZrSe}_2$  and  $\text{ZrS}_2$  using polarization-resolved Raman measurements and DFT-calculated phonon dispersion curves. We track the evolution in the primary Raman-active modes with alloying and find that they exhibit two-mode behavior, and we observe the activation of many new phonons present only in the alloys. While some of these features are activated due to either broken translational symmetry or different configurations of chalcogen atoms that introduce new vibrations, comparison with our recently developed method for simulating Raman spectra in alloys<sup>26</sup> reveals that many of these features originate from forbidden IR phonons. This is attributed to the high ionicity in the intralayer chemical bonds. SE measurements of the complex refractive index identify the first three direct, allowed optical transitions and quantify their blue-shift with increasing S content. By comparing these data to electronic structure calculations, we estimate that the  $\Gamma$ -point exciton binding energy is in the range of 200 meV for  $\text{ZrS}_2$  and  $\text{ZrSe}_2$ . For near-infrared (NIR) light below the direct band gap,  $\text{ZrS}_x\text{Se}_{2-x}$  materials feature strong light-matter interaction ( $n \gtrsim 2$ ) and rather low optical loss ( $k \lesssim 0.5$ ) that decrease with increasing S content, which may be particularly useful for making atomically-thin NIR photonic devices. This study offers a roadmap for the application of  $\text{ZrS}_x\text{Se}_{2-x}$  alloys in high-performance photonics technologies.<sup>27</sup>

## 2 Experimental and theoretical methods

### 2.1 Material growth

Synthesis of layered  $\text{ZrS}_x\text{Se}_{2-x}$  alloy flakes is achieved using the chemical vapor transport (CVT) method. Source materials are loaded into a quartz ampoule with an inner diameter of 10 mm and a 2 mm wall thickness, which is also loaded with  $\text{I}_2$  as the CVT transport agent at a concentration of  $5 \text{ mg cm}^{-3}$ . The ampoules are then evacuated with a turbo pump to a pressure of approximately  $10^{-5}$  Torr and sealed with an oxy-hydrogen torch to a total length of 180 mm.

Two Zr source options are employed independently as side-by-side comparisons of metal sources on crystal growth dynamics, which we elaborate upon in detail below. The two sources include a fine grain –325 mesh powder (Sigma-Aldrich, Product #756385-5G 99.5% metals basis, excluding Hf) and the other is a bulk 3–6 mm Zr lump source (Alfa Aesar, Product #36253 99.8% metals basis, excluding Hf) combined with chalcogen sources comprising Se powder (Alfa Aesar, Product #036208, –200 mesh 99.999% metals basis) and S pieces (Alfa Aesar, Product #10755, Puratronic 99.999% metals basis).

One will note the presence of Hf contained within the two Zr sources as a natural impurity that cannot be refined beyond the purification process absent of extensive effort and monetary expense. The Hf content in the lot of Zr powder utilized in the growths is provided as 1.8 molar %. Likewise, the Zr lump source Hf content is provided as 1.4 molar %. Therefore, one may expect the presence of Hf at a considerable level beyond a moderate or high-doping concentration as an impurity constituent in the  $\text{ZrS}_x\text{Se}_{2-x}$  flakes grown.

A four-zone tube furnace is used for growth by heating two zones to maintain a hot-zone temperature of  $900^\circ\text{C}$  and the other two zones to achieve a reaction zone temperature of  $800^\circ\text{C}$ . A ceramic center baffle is fitted to provide a sharp temperature gradient. Prior to heating to the CVT gradient temperatures, an intermediate temperature dwell at  $450^\circ\text{C}$  is held for 24 hours in order to initiate an equilibrium of S vapor sublimation and allow for metal–chalcogen pre-reactions and source compounding to occur. The temperature gradient of  $900/800^\circ\text{C}$  is used for all growths and is found to optimize the transport product density and enhance the size of the flakes produced.

Regarding growth dynamics (to be discussed in more detail in a forthcoming publication), we find that Zr lump sources loaded into the growth ampoule yield the desired  $\text{ZrS}_x\text{Se}_{2-x}$  dichalcogenide phase, whereas Zr powder sources yield the  $\text{ZrS}_x\text{Se}_{3-x}$  trichalcogenide phase with consistent repeatability. It has been suggested that the morphology of Zr source particles and native oxide shells can influence the Zr sublimation and vapor transport rate which consequently impacts the vapor-phase stoichiometry at the reaction zone of the growth ampoule. As a result, a chalcogen-rich vapor phase is suspected to produce the Zr-trichalcogenide structure due to limited Zr sublimation from utilizing fine grain Zr source particles with a much higher surface to volume ratio relative to the larger Zr lump pieces. For the  $\text{ZrS}_x\text{Se}_{2-x}$  dichalcogenide crystals used in this study, the resultant flake compositions match reasonably well with the nominal source stoichiometries (targeted compositions  $x = 0, 0.2, 0.5, 0.8, 1.0, 1.2, 1.5, 1.8, 2.0$ ) by achieving approximate compositional values of  $x = 0, 0.15, 0.3, 0.6, 1.05, 1.14, 1.51, 1.8$  and  $2.0$ .

### 2.2 Computational details

All calculations are carried out using Vienna Ab initio Simulation Package (VASP).<sup>28,29</sup> The atomic structures are optimized using revB86b functional,<sup>30</sup> which has been shown to reproduce the experimental lattice parameters and also provide reasonable interlayer binding energies.<sup>31</sup> Here, we use 400 eV plane wave cut-off and  $12 \times 12 \times 4$  mesh for sampling the Brillouin zone of the primitive cell. The lattice constants, direct and indirect band gaps, and dielectric constants are collected in Tables 1–3.

Electronic structures are calculated on top of the revB86b-optimized structure using PBE,<sup>32</sup> HSE06,<sup>33,34</sup> G0W0, and GW0 levels of theory, in addition to revB86b results. Following an approach similar to that described by Klimes *et al.*,<sup>35</sup> our final QP energies are obtained by combining a calculation at a more accurate  $k$ -point mesh with a medium basis-set size and a

**Table 1** Bulk lattice constants  $a$  and  $c$  as calculated with the revB86b functional and compared to experimental values

	Expt. $a$ (Å)	Calc. $a$ (Å)	Expt. $c$ (Å)	Calc. $c$ (Å)
ZrS <sub>2</sub>	3.63–3.66	3.660	5.81–5.85	5.829
ZrSe <sub>2</sub>	3.77–3.80	3.768	6.14–6.19	6.155

**Table 2** Minimum indirect and direct band gaps calculated using revB86b, PBE, HSE06, G0W0, and GW0 on top of the revB86b optimized structure

	revB86b (eV)	PBE (eV)	HSE06 (eV)	G0W0 (eV)	GW0 (eV)
ZrS <sub>2</sub>	Indirect 0.78	0.80	1.61	1.79	1.98
	Direct 1.46	1.49	2.39	2.59	2.81
ZrSe <sub>2</sub>	Indirect 0.18	0.19	0.86	1.02	1.20
	Direct 1.01	1.04	1.81	1.97	2.16

**Table 3** Electronic part of the dielectric constant calculated using revB86b, PBE, and GW0, and the ionic part calculated using PBE, all on top of the revB86b optimized structure. The two values correspond to the component parallel and perpendicular to the sheet

	Electronic part			Ionic part
	revB86b	PBE	GW0	PBE
ZrS <sub>2</sub>	11.71/6.04	11.52/5.87	10.86/5.48	40.45/0.74
ZrSe <sub>2</sub>	17.78/8.88	17.47/8.42	15.83/7.72	64.50/0.80

correction based on a set of calculations at a coarser  $k$ -point mesh with few different basis-set sizes, from which we extrapolate to the limit of an infinitely large basis set. In the latter, we use  $6 \times 6 \times 4$   $k$ -point mesh and plane wave basis cut-offs of 282.4, 353.5, 448.3 eV. The first is the recommended value for the set of PAWs used here (\_GW variants), and the other after scaling by a factor of 1.25 and 1.587.<sup>35</sup> Concurrently, we also scale the number of states in the calculations and the cut-off for describing the response functions. Throughout, we use 50% of the total number of states that can be described using a selected plane wave cut-off. The cut-off for the response functions is half of the wave function cut-off. Extrapolation is carried out assuming that QP energies converge as  $(1/E_{\text{cut}})^{3/2}$ . The corrections are less than 50 meV. The finer mesh calculation is carried out using  $12 \times 12 \times 6$   $k$ -point mesh and the other parameters set similar to the 353.5 eV cut-off calculation.

revB86b and PBE appear to yield very similar results for the electronic structure, but the band gaps are dramatically underestimated. HSE06 improves on the band gaps, but they are still underestimated. In the case of ZrS<sub>2</sub>, G0W0 (indirect gap) of 1.79 eV is fairly close to the experimental gap of 1.7 eV, whereas GW0 seems to yield too large of a band gap. On the other hand, in the case of ZrSe<sub>2</sub>, the GW0 gap of 1.20 eV matches the experimental gap of 1.2 eV. Without diving more deeply into the possible origins of the discrepancy, since previous investigations for larger material sets have concluded GW0 to yield slightly better agreement with experimental gaps than G0W0, we use those values to realign the calculated band gaps.

The dielectric constants are calculated within the density functional perturbation theory approach. revB86b and PBE functionals yield again very similar results, and also the GW results for the electronic contribution are similar. We find extremely large ionic contribution to the dielectric constants, which leads to large  $\epsilon_0/\epsilon_\infty$  ratio and thereby to large longitudinal optical (LO)–transverse optical (TO) phonon splitting.

The mixing energies of alloys are studied using cluster expansion fitted to a set of DFT energies, as automated in the Alloy Theoretic Automated Toolkit (ATAT) package.<sup>36–38</sup> Since the cluster expansion study indicates very low mixing energies (well below  $k_B T$  at room temperature), the S and Se atoms in the alloy should be randomly mixed. The lattice constants and band gaps of the alloys are evaluated using special quasi-random structure (SQS) within  $4 \times 4 \times 2$  supercells.

The simulated Raman spectra are evaluated using the RGDOS approach recently introduced in ref. 26. The force constant matrix and phonon dispersion curves for the pristine systems are built with Phonopy<sup>39</sup> using  $8 \times 8 \times 3$  supercell. The vibrational modes of the alloy supercells are evaluated by mass approximation, *i.e.*, we use the force constants of ZrS<sub>2</sub> and only account for the mass difference between S and Se atoms. We use  $8 \times 8 \times 3$  supercells with randomly substituted S and Se atoms, and average over 10 instances of random substitution. The Raman tensors are calculated from the change of dielectric constant with the displacement along the vibrational eigenmodes. Due to the large long-range Coulomb interactions in this material (to be discussed in detail later), we have also included the non-analytic corrections to the dynamical matrix in the case of alloys. Since force constants are fixed to that of ZrS<sub>2</sub>, we also use for all atoms the Born effective charges from pristine ZrS<sub>2</sub>.

### 2.3 Optical studies

For Raman studies, ZrS<sub>x</sub>Se<sub>2–x</sub> crystals are mechanically exfoliated and bulk flakes are deposited onto SiO<sub>2</sub>/Si substrates with a 90 nm oxide thickness. Raman measurements are performed on a home-built confocal microscope in a backscattering geometry that is integrated with a single closed-cycle cryostation. The excitation source for the Raman measurements is a 532 nm laser focused through a 0.42 NA long working distance objective with 50 $\times$  magnification. The spot size is  $\approx 2.4$   $\mu\text{m}$  in diameter and the laser power density is fixed at 442  $\mu\text{W } \mu\text{m}^{-2}$ . Collected light is directed to a 500 mm focal length spectrometer with a liquid nitrogen-cooled CCD. The spectrometer and camera are calibrated using a Hg–Ar atomic line source. For spectral analysis, the Raman peaks are fit with Lorentzian profiles.

Polarization-resolved Raman measurements are carried out by inserting a half-wave plate into the experimental setup to control the excitation polarization. A linear polarizer is used to selectively collect backscattered light that is either co-polarized or cross-polarized with the excitation source. The polarized Raman data is normalized by exposure time and a polarization bias of the optics is accounted for.

We perform SE measurements using an M-2000 instrument from J. A. Woollam. The instrument uses a rotating compensator

configuration as shown in the ESI,<sup>†</sup> Fig. S1, and consists of the following elements in consecutive order: broadband white light source, polarizer, rotating compensator, micro-spot objective projecting the light onto the sample, analyzer, and detector (CCD-based multi-channel for visible light). The focusing optics have a spot size of  $\approx 300\ \mu\text{m}$  at  $70^\circ$  angle of incidence.

For the SE studies, the bulk crystals are stored in ambient conditions and can be expected to have native oxide surfaces. We use tape (Scotch 810 Magic from 3M) to gently remove the topmost layers of material and expose fresh surfaces before SE measurements. The measurements are performed within 10 minutes of this surface preparation, during which time we expect the growth of a native oxide layer of thickness  $\approx 0.5\ \text{nm}$  (to be published later), which we incorporate in our SE data analysis.

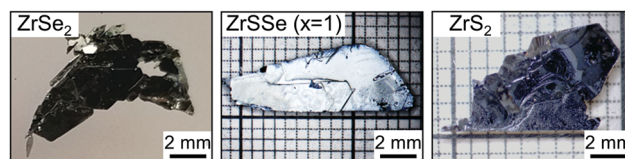
### 3 Results and discussion

#### 3.1 Material growth, structural characterization, and density functional theory

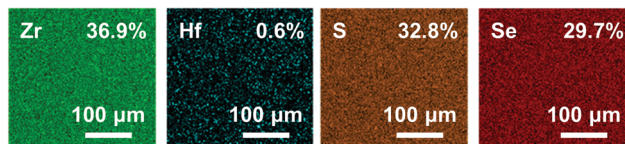
$\text{ZrS}_x\text{Se}_{2-x}$  alloys are grown using the CVT method with  $\text{I}_2$  as the transport agent. Resultant bulk flakes had lateral sizes in excess of 10 mm for all compositions, as shown for select samples in the optical images of Fig. 1a. Energy-dispersive X-ray spectroscopy (EDS) mapping was used to determine the alloy composition  $x$  values, and we also found a homogeneous chalcogen mixing (Fig. 1b). Trace amounts of Hf impurities were also detected in the EDS measurements at levels of  $\approx 0.2$ – $0.6$  molar %. This level of source contamination is low enough to not significantly affect the results of our study. Further details regarding Hf impurities and the growth process can be found in the *Experimental and theoretical methods* section. The pure components of the  $\text{ZrS}_x\text{Se}_{2-x}$  alloy system,  $\text{ZrS}_2$  ( $x = 2$ ) and  $\text{ZrSe}_2$  ( $x = 0$ ), crystallize in the 1T structure ( $D_{3d}$  point group, space group  $P\bar{3}m1$ , #164) at ambient temperature and pressure (Fig. 1c). Therefore, the  $\text{ZrS}_x\text{Se}_{2-x}$  system is isostructural and is expected to form a full solid solution in the 1T phase as previously reported.<sup>19</sup> Our EDS results support this expectation, and our X-ray diffraction (XRD) and Raman spectra cannot be modeled as linear superpositions of the parent compounds which is strong evidence against nanoscale binary phase separation. See the ESI,<sup>†</sup> Fig. S2, for XRD results of select alloys.

DFT calculations shown in Fig. 2 demonstrate the effects of alloying on the mixing energies, lattice constants, and band gaps of  $\text{ZrS}_x\text{Se}_{2-x}$ . The mixing energies presented in Fig. 2a are calculated using cluster expansion (CE) fitted to a set of DFT energies. Since the CE results indicate very low mixing energies (well below  $k_B T$  at room temperature), the S and Se atoms in the alloy should be randomly mixed. An interesting observation is that the convex hull shows that there is, in principle, a stable  $\text{ZrSSe}$  phase ( $x = 1$ ) with Janus distribution.<sup>40,41</sup> However, the energy gain is so small that this is unlikely to show up in our samples. In Fig. 2b we display the effects of alloying on the  $a$  and  $c$  lattice constants. Here, the points in the plot are from all of the different structures used to train CE and the line is

(a) CVT-prepared layered bulk crystals



(b) EDS mapping and atomic % quantifications for a  $\text{ZrSSe}$  alloy



(c) 1T-phase  $\text{ZrX}_2$  Structure ( $X = \text{Se or S}$ )

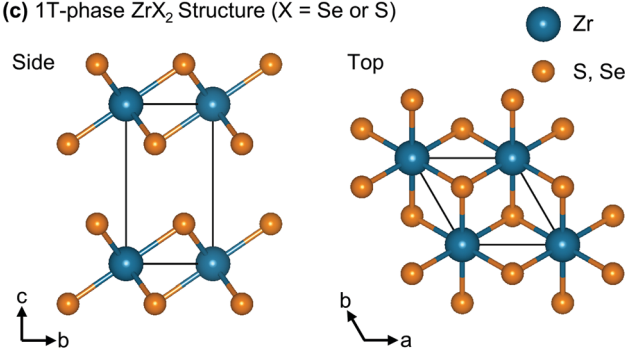


Fig. 1 (a) Optical images of select bulk  $\text{ZrS}_x\text{Se}_{2-x}$  crystals obtained through the chemical vapor transport (CVT) process. Lateral sizes extend in excess of 10 mm for all compositions. The scale bar is 2 mm. (b) Energy-dispersive X-ray spectroscopy (EDS) mapping indicating atomic % quantifications for a  $\text{ZrSSe}$  ( $x = 1$ ) flake and showing homogeneous chalcogen mixing distribution along with Hf presence as a source impurity constituent. The scale bar is  $100\ \mu\text{m}$ . (c) Side and top view of the 1T crystal structure of  $\text{ZrX}_2$  ( $X = \text{Se or S}$ ). The black lines indicate the unit cell.

from the special quasi-random structure (SQS) that is constructed to mimic random alloys. Lattice constant  $a$  is found to behave linearly, evolving from  $3.76\ \text{\AA}$  in  $\text{ZrSe}_2$  to  $3.65\ \text{\AA}$  in  $\text{ZrS}_2$ , while lattice constant  $c$  has a small upward bowing and which evolves from  $6.12\ \text{\AA}$  in  $\text{ZrSe}_2$  to  $5.80\ \text{\AA}$  in  $\text{ZrS}_2$ . Lastly, Fig. 2c shows the calculated indirect band gaps of the  $\text{ZrS}_x\text{Se}_{2-x}$  alloys. After applying the GW correction to the SQS, the calculated band gaps showed small bowing and are in good agreement with those determined experimentally in ref. 6.

#### 3.2 Phonons

Raman measurements of bulk  $\text{ZrS}_x\text{Se}_{2-x}$  flakes taken at 5 K (Fig. 3a) are used to explore the effects of alloying on the phonon modes. These low-temperature measurements minimize thermal broadening and allow for a more direct comparison with our theoretical calculations at 0 K. For a comparison of Raman spectra for the  $\text{ZrS}_x\text{Se}_{2-x}$  alloys taken at both 300 K and 5 K, see the ESI,<sup>†</sup> Fig. S3. We track the evolution in the 5 K Raman modes with alloying in Fig. 3b by fitting the spectra with multiple Lorentzians to extract peak frequencies. See the ESI,<sup>†</sup> Fig. S4, for examples of Lorentzian fits to select alloys.

We first examine the spectra of the endpoint compounds  $\text{ZrS}_2$  and  $\text{ZrSe}_2$  that are shown in blue in Fig. 3a. Our interpretation



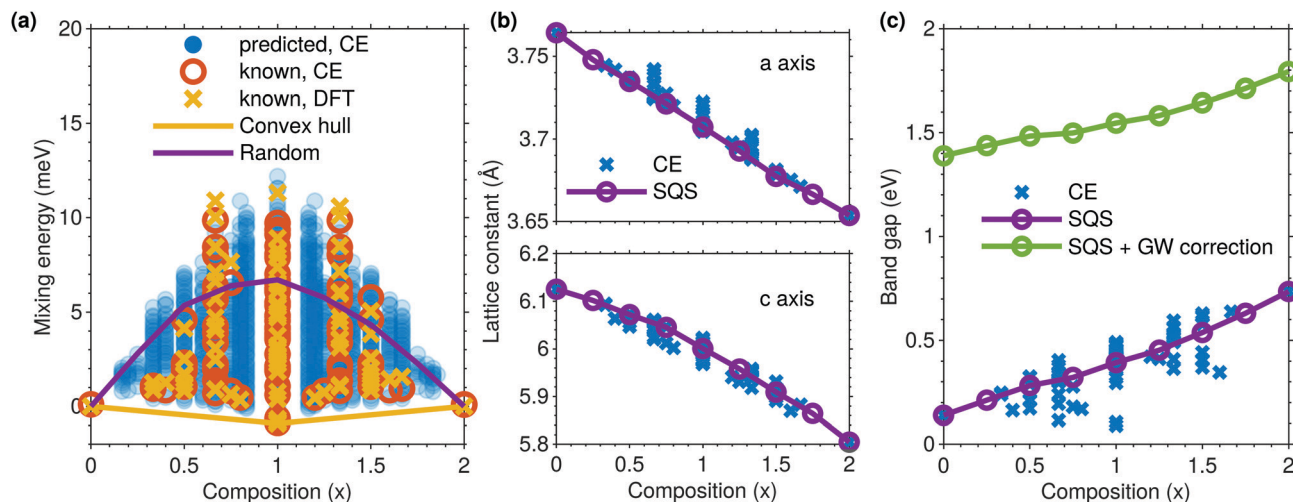


**Fig. 2** (a) Mixing energies of  $\text{ZrS}_x\text{Se}_{2-x}$  as a function of alloy composition  $x$ . Filled blue circles denote energies predicted using cluster expansion (CE) of all symmetrically inequivalent structures with less than 18 atoms in the unit cell. Energies of the structures that were used to fit CE are highlighted with red circles and the corresponding DFT-calculated values are shown with yellow crosses. All energies are well below  $k_B T$  at room temperature indicating that the S and Se distributions are completely random. (b) The alloy dependence of the  $a$  and  $c$  lattice parameters (top and bottom panels, respectively). The points are from all the different structures used to train CE and the line is from the special quasi-random structure (SQS). (c) Calculated indirect band gaps of the  $\text{ZrS}_x\text{Se}_{2-x}$  alloys. Application of the GW correction to SQS more accurately predicts the band gap values from the literature.<sup>6</sup>

of this data is guided by DFT modeling of the phonon dispersion curves for  $\text{ZrS}_2$  and  $\text{ZrSe}_2$  in Fig. 3c and d, respectively. Since both compounds crystallize in the 1T phase, they share the same irreducible representation of optical phonons at the center of the Brillouin zone ( $\Gamma$  point), given by

$$\Gamma_{\text{bulk}} = A_{1g} + E_g + 2A_{2u} + 2E_u. \quad (1)$$

The modes with  $A_{1g}$  and  $E_g$  symmetry are Raman-active and correspond to vibrations of the chalcogen atoms that occur either out-of-plane or in-plane, respectively, while the transition metal atoms remain stationary. Meanwhile, the  $A_{2u}$  and  $E_u$  modes are IR-active and correspond to vibrations of the chalcogen and transition metal atoms either out-of-plane or in-plane, respectively. There are a total of 9 phonons since the  $E_g$  and  $E_u$  symmetry modes are doubly degenerate at the  $\Gamma$  point.

Polarization-resolved Raman measurements (ESI,† Fig. S5) assist DFT phonon modeling in distinguishing between the Raman-active  $A_{1g}$  and  $E_g$  symmetry modes. For these measurements, the sample is excited with linearly-polarized light, and the detected, back-scattered light is either co-polarized ( $\parallel$ ) or cross-polarized ( $\perp$ ) with the excitation light. Due to the differing Raman tensors for the  $A_{1g}$  and  $E_g$  modes,  $A_{1g}$  modes should only be present in the  $\parallel$  configuration whereas  $E_g$  modes should be present in both the  $\parallel$  and  $\perp$  configurations. We note that there is some signature of the  $A_{1g}$  modes in the  $\perp$  configuration due to imperfection of the polarizing optics.

We observe 8 peaks in the Raman measurements of  $\text{ZrS}_2$  ( $x = 2$ ) at 5 K that are labeled with letters a–h in the left and right panels of Fig. 3a. The frequencies and symmetry assignments of these features are listed in Table 4. Peak a is measured at  $254 \text{ cm}^{-1}$  and is assigned to the Raman-active  $E_g$  mode that we calculate at  $248 \text{ cm}^{-1}$ , which agrees with previous

theoretical<sup>42</sup> and experimental results.<sup>43</sup> This assignment is also supported by our polarization-resolved Raman measurements in the ESI,† Fig. S4, that detect the  $254 \text{ cm}^{-1}$  feature in both the  $\parallel$  and  $\perp$  configurations. The dominant feature centered at  $\approx 325 \text{ cm}^{-1}$  is shown in our polarized Raman measurements to be present in the  $\parallel$  configuration, but it is significantly decreased in intensity in the  $\perp$  configuration, which suggests that it has  $A_{1g}$  symmetry. We discuss this feature in detail below.

The dominant feature that we measure in  $\text{ZrS}_2$  at  $\approx 325 \text{ cm}^{-1}$  exhibits broad asymmetry. We can model this feature using three Lorentzians centered at  $320 \text{ cm}^{-1}$  (peak b),  $325 \text{ cm}^{-1}$  (peak c), and  $331 \text{ cm}^{-1}$  (peak d), as shown in the ESI,† Fig. S6. Prior studies have attributed the asymmetric lineshape of this feature to anharmonic effects such as the decay of an  $A_{1g}$  optical phonon into low-energy acoustic phonons.<sup>45</sup> Earlier studies, however, suggested its broadness and asymmetry is the result of dipolar interactions that mix the Raman-active  $A_{1g}$  phonon with nearly degenerate IR-active phonons.<sup>43,44</sup> The dipolar interactions result from Zr belonging to group IVB, which causes the intralayer chemical bonds to have a more ionic character,<sup>43,46</sup> as evidenced by our theoretical calculations that show an extremely large ionic contribution to the dielectric constants given by a high  $\epsilon_0/\epsilon_\infty$  ratio (see *Experimental and theoretical methods* section). This is in contrast to the more commonly studied group VIB TMDs (*i.e.*, containing Mo and W) that have predominantly covalent intralayer chemical bonds. The highly ionic nature of  $\text{ZrS}_2$  gives rise to long-range Coulomb interactions that have a significant effect on lattice dynamics.<sup>43</sup> Not only do the long-range forces result in the  $A_{1g}$  and  $E_g$  modes having a larger frequency difference than expected, but they also lead to a considerable LO–TO splitting and anisotropy of the IR phonons.<sup>43</sup> As shown in Fig. 3c, incorporation of

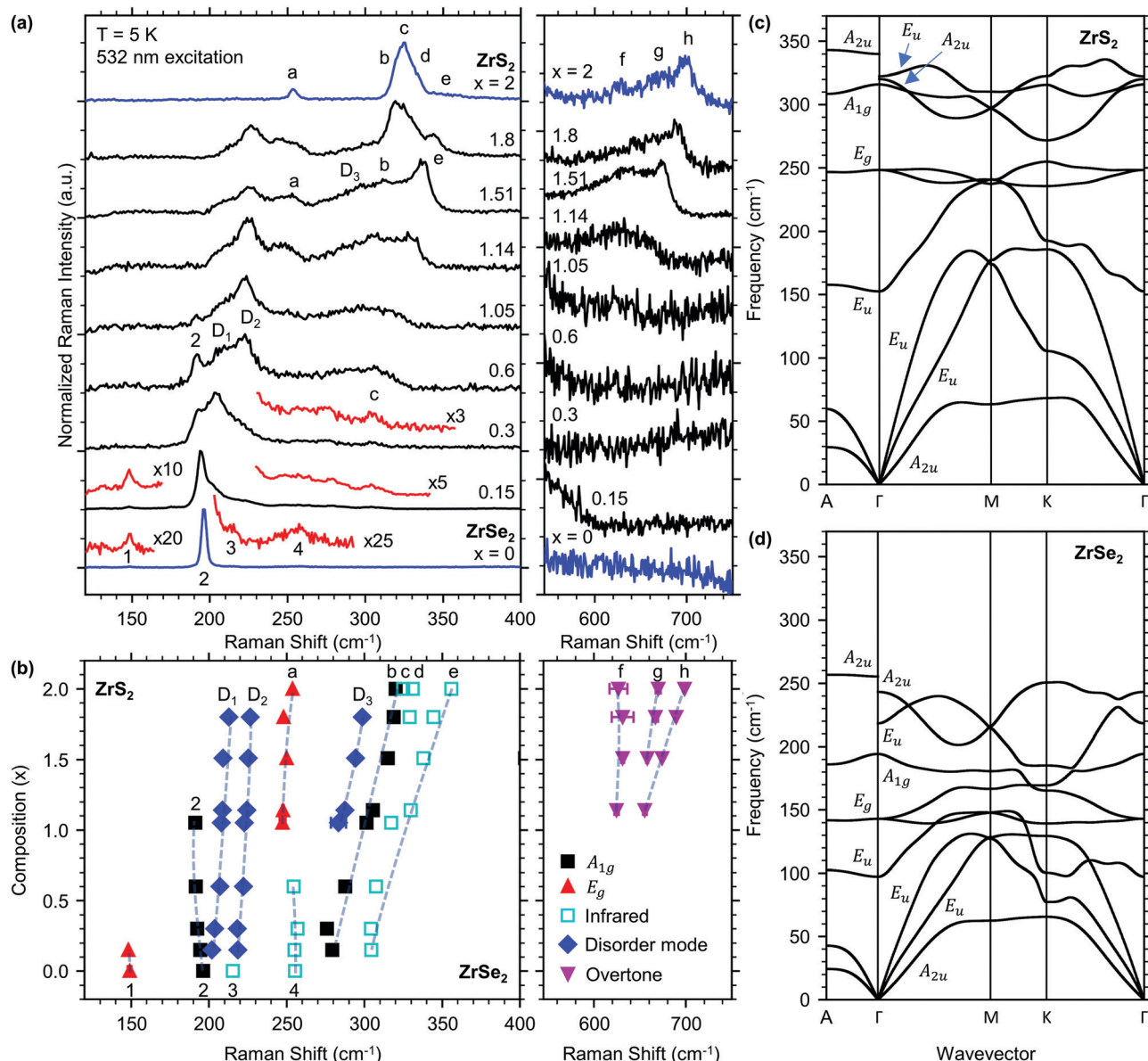


**Fig. 3** (a) Unpolarized Raman spectra of bulk  $\text{ZrS}_x\text{Se}_{2-x}$  alloys ( $x = 0 \dots 2$ ) taken at 5 K with 532 nm excitation. Portions of the spectra have been scaled for clarity (red curves). The vibrational modes of the endpoint compounds  $\text{ZrSe}_2$  and  $\text{ZrS}_2$  are identified with numbers and letters, respectively, and their experimental frequencies and symmetry assignments are listed in Table 4. (b) Evolution in the Raman mode frequencies with alloying. The peak frequencies are extracted from Lorentzian fits to the data displayed in panel (a). (c) Calculated phonon dispersion curves for (c)  $\text{ZrS}_2$  and (d)  $\text{ZrSe}_2$ . Error bars in panel (b) are equal to one standard deviation.

long-range Coulomb interactions into our phonon dispersion calculations yields a large LO-TO splitting of the  $E_u$  phonons for in-plane wavevector  $q$ , which is along the  $\Gamma$ - $M$ - $K$ - $\Gamma$  direction. The  $E_u(\text{TO})$  mode is at  $152 \text{ cm}^{-1}$  and the  $E_u(\text{LO})$  mode is at  $322 \text{ cm}^{-1}$ , which gives an LO-TO splitting of  $170 \text{ cm}^{-1}$  that agrees with previous results in the literature.<sup>42,47</sup> For out-of-plane  $q$ , which is along the  $\Gamma$ - $A$  direction, the degenerate  $E_u(\text{LO/TO})$  mode is at  $152 \text{ cm}^{-1}$ . Long range Coulomb interactions are anisotropic due to differences between in-plane *versus* out-of-plane screening, which leads to a discontinuity in the  $A_{2u}$  mode dispersion at the  $\Gamma$  point. The  $A_{2u}(\text{TO})$  mode approaches  $320 \text{ cm}^{-1}$  as  $q$  goes from  $M \rightarrow \Gamma$ , while the  $A_{2u}(\text{LO})$  mode reaches a value of  $340 \text{ cm}^{-1}$  for

$q$  from  $A \rightarrow \Gamma$ . These results demonstrate that the  $A_{1g}$  mode, which is at  $316 \text{ cm}^{-1}$  at the  $\Gamma$  point, is accompanied by  $A_{2u}$  and  $E_u$  modes at slightly higher frequencies, as pointed out by arrows in the  $\text{ZrS}_2$  phonon band structure of Fig. 3c. We suggest that these findings support previous assignments of the large and broad  $\text{ZrS}_2$  Raman feature to hybridization of the Raman-active  $A_{1g}$  phonon with nearly degenerate IR phonons that is driven by dipolar interactions.<sup>43,44</sup> Peak b is assigned to the  $A_{1g}$  mode and peak c is assigned to the  $A_{2u}(\text{TO})$  mode, as has been done in ref. 43 where the authors have also accounted for long-range Coulomb terms in their phonon calculations. Peak d is assigned to the  $E_u(\text{LO})$  mode, which agrees with both our  $\text{ZrS}_2$

**Table 4** ZrS<sub>2</sub> and ZrSe<sub>2</sub> vibrational mode frequencies and symmetry assignments for the peaks identified in low-temperature Raman spectra (*T* = 5 K). The peak labels, which are either letters or numbers, refer to the ZrS<sub>2</sub> and ZrSe<sub>2</sub> Raman features in Fig. 3a.  $\omega_{\text{exp}}$  are experimentally determined frequencies, whereas  $\omega_{\text{cal}}$  are DFT-calculated frequencies. The superscript \* refers to assignments made in this work, while the superscripts  $\alpha$  and  $\beta$  refer to assignments made in ref. 43 and 44

Label	$\omega_{\text{exp}}$ (cm <sup>-1</sup> )	$\omega_{\text{cal}}$ (cm <sup>-1</sup> )	Assignment
ZrS <sub>2</sub> ( <i>x</i> = 2)			
		152	E <sub>u</sub> (TO)
a	254	248	E <sub>g</sub>
b	320	316	A <sub>1g</sub>
c	325	320	A <sub>2u</sub> (TO)
d	331	322	E <sub>u</sub> (LO)
e	356	340	A <sub>2u</sub> (LO)
f	627		2A <sub>1g</sub> * or [E <sub>u</sub> (LO) + A <sub>2u</sub> (TO)] <sup>α</sup>
g	670		2E <sub>u</sub> (LO)*, [E <sub>u</sub> (LO) + A <sub>2u</sub> (LO)]*, or 2A <sub>2u</sub> (LO) <sup>α</sup>
h	699		2A <sub>2u</sub> (LO)* or 2E <sub>u</sub> (LO) <sup>α,β</sup>
ZrSe <sub>2</sub> ( <i>x</i> = 0)			
		97	E <sub>u</sub> (TO)
1	149	143	E <sub>g</sub>
2	196	194	A <sub>1g</sub>
3	215	218	E <sub>u</sub> (LO)
4	256	243 or 255	A <sub>2u</sub> (TO) or A <sub>2u</sub> (LO)

phonon dispersion curves as well as previous calculations<sup>43</sup> and experiment.<sup>44</sup>

The remaining features in ZrS<sub>2</sub>, labeled peaks e–h in Fig. 3a, are attributed to IR and overtone modes. Peak e is very weak and is measured at 356 cm<sup>-1</sup> (see the ESI,† Fig. S6, for a clearer view). As discussed previously, we find that incorporation of long-range Coulomb interactions in our ZrS<sub>2</sub> phonon dispersion calculations yields anisotropy of IR modes. Close inspection of Fig. 3c shows that the phonon band structure is spectrally clean in this frequency range for in-plane *q*. However, we calculate an IR-active A<sub>2u</sub>(LO) mode for out-of-plane *q* (*Γ*–*A* direction), and so we assign peak e to this feature. Lastly, peaks f, g, and h are measured at 627 cm<sup>-1</sup>, 670 cm<sup>-1</sup>, and 699 cm<sup>-1</sup>, respectively (top blue curve in the right panel of Fig. 3a). These features have been previously explored in resonant Raman studies and are assigned to IR combination modes.<sup>43,44</sup> Possible assignments of these features are listed in Table 4.

Next, we examine the 5 K Raman data for ZrSe<sub>2</sub> (*x* = 0), which reveals 4 peaks that are labeled with numbers in Fig. 3a. The experimentally determined frequencies and symmetry assignments for these features are listed in Table 4. Peak 1 and peak 2 are measured at 149 cm<sup>-1</sup> and 196 cm<sup>-1</sup>, and are assigned to the Raman-active E<sub>g</sub> and A<sub>1g</sub> modes that we calculate at 143 cm<sup>-1</sup> and 194 cm<sup>-1</sup> at the *Γ* point, respectively (Fig. 3d). These assignments agree with results previously recorded in the literature<sup>45</sup> and are supported by our polarized Raman measurements found in the ESI,† Fig. S5. The features measured at 215 cm<sup>-1</sup> (peak 3) and 256 cm<sup>-1</sup> (peak 4) are very weak, and so are not easily resolvable unless scaled as we have done in the red curves of Fig. 3a. Both of these peaks have been seen in previous Raman measurements of ZrSe<sub>2</sub>,<sup>45,48</sup> but no comment was made on the appearance of peak 3 whereas peak 4 was suggested to originate from a two phonon state.<sup>45</sup> Here, our ZrSe<sub>2</sub>

phonon band calculations in Fig. 3d, in which we incorporate the long-range Coulomb interactions discussed previously due to the presence of Zr, show LO–TO splitting of the IR-active E<sub>u</sub> phonons and anisotropy of the A<sub>2u</sub> phonons. These results let us assign peak 3 to an E<sub>u</sub> mode calculated at 218 cm<sup>-1</sup> and peak 4 to either an A<sub>2u</sub>(TO) mode at 243 cm<sup>-1</sup> or an A<sub>2u</sub>(LO) mode at 255 cm<sup>-1</sup>. The larger energy difference between the A<sub>1g</sub>, E<sub>u</sub>, and A<sub>2u</sub> modes for ZrSe<sub>2</sub> suppresses mixing and explains why the A<sub>1g</sub> mode is narrow in contrast to ZrS<sub>2</sub>.

Now that the vibrational modes of the endpoint compounds ZrS<sub>2</sub> and ZrSe<sub>2</sub> have been identified, we combine polarization-resolved Raman measurements and simulated Raman and IR spectra to track their evolution with alloying. This analysis is demonstrated for *x* = 0.6 and *x* = 1.51 in Fig. 4a and b, respectively. See the *Experimental and theoretical methods* section for computational details regarding our method for simulating Raman spectra of alloys<sup>26</sup> and the ESI,† Fig. S7, for Raman spectra calculated across the entire compositional range. Polarization-resolved Raman measurements of other alloy compositions can be found in the ESI,† Fig. S5. In both panels of Fig. 4, the ZrSe<sub>2</sub> and ZrS<sub>2</sub> features are labeled with the same numbers and letters found in Fig. 3a and b and they are accompanied by vibrational mode symmetry assignments.

Alloying has significant effect on the vibrational modes detected in ZrS<sub>2</sub> and ZrSe<sub>2</sub>. The Raman-active E<sub>g</sub> and A<sub>1g</sub> modes, represented by red triangles and black squares in Fig. 3b, respectively, exhibit two-mode behavior. This phenomenon is classified by a superposition of peaks with like symmetries from the alloy end components together in the same spectrum that have intensities proportional to the mole fraction of their respective parent compound.<sup>49</sup> One-mode behavior, on the other hand, is characterized by the continuous shift of a single peak from the frequency of one endpoint to that of the other with little to no change in intensity.<sup>49</sup> Two-mode behavior has been studied in the Raman spectra of the very similar HfS<sub>2(1-x)</sub>Se<sub>2x</sub><sup>50</sup> and SnS<sub>x</sub>Se<sub>2-x</sub><sup>51</sup> systems as well as in other TMD alloys.<sup>12,52,53</sup> Although there remains significant work to be done for obtaining a full understanding of the criteria that yields two-mode behavior, it is worth emphasizing that this property is well-known to occur in mixed crystals and is not necessarily a sign of phase separation.<sup>49,54–56</sup> Here, we find that the ZrS<sub>x</sub>Se<sub>2-x</sub> alloys do not fulfill a requirement for two-mode behavior that the mass of the substituting element (*S* in this case, 32 amu) must be smaller than the reduced mass of the compound formed by the other two elements (ZrSe<sub>2</sub> in this case, ≈29 amu).<sup>49,56</sup> However, close inspection of the phonon dispersion curves for ZrS<sub>2</sub> and ZrSe<sub>2</sub> in Fig. 3c and d reveals that the A<sub>1g</sub> and E<sub>g</sub> modes are separated by 124 cm<sup>-1</sup> and 105 cm<sup>-1</sup> at the *Γ* point, respectively, and that these bands never overlap in frequency for finite momentum. The same analysis was done for SnS<sub>x</sub>Se<sub>2-x</sub><sup>51</sup> and suggests that no mixing of these features should occur so that one-mode behavior is not expected for the A<sub>1g</sub> and E<sub>g</sub> modes.

Most of the IR modes in ZrS<sub>2</sub> and ZrSe<sub>2</sub> are unresolvable with light doping (cyan squares of Fig. 3b). This may be due to a higher signal to noise ratio in the alloys or otherwise an overlap



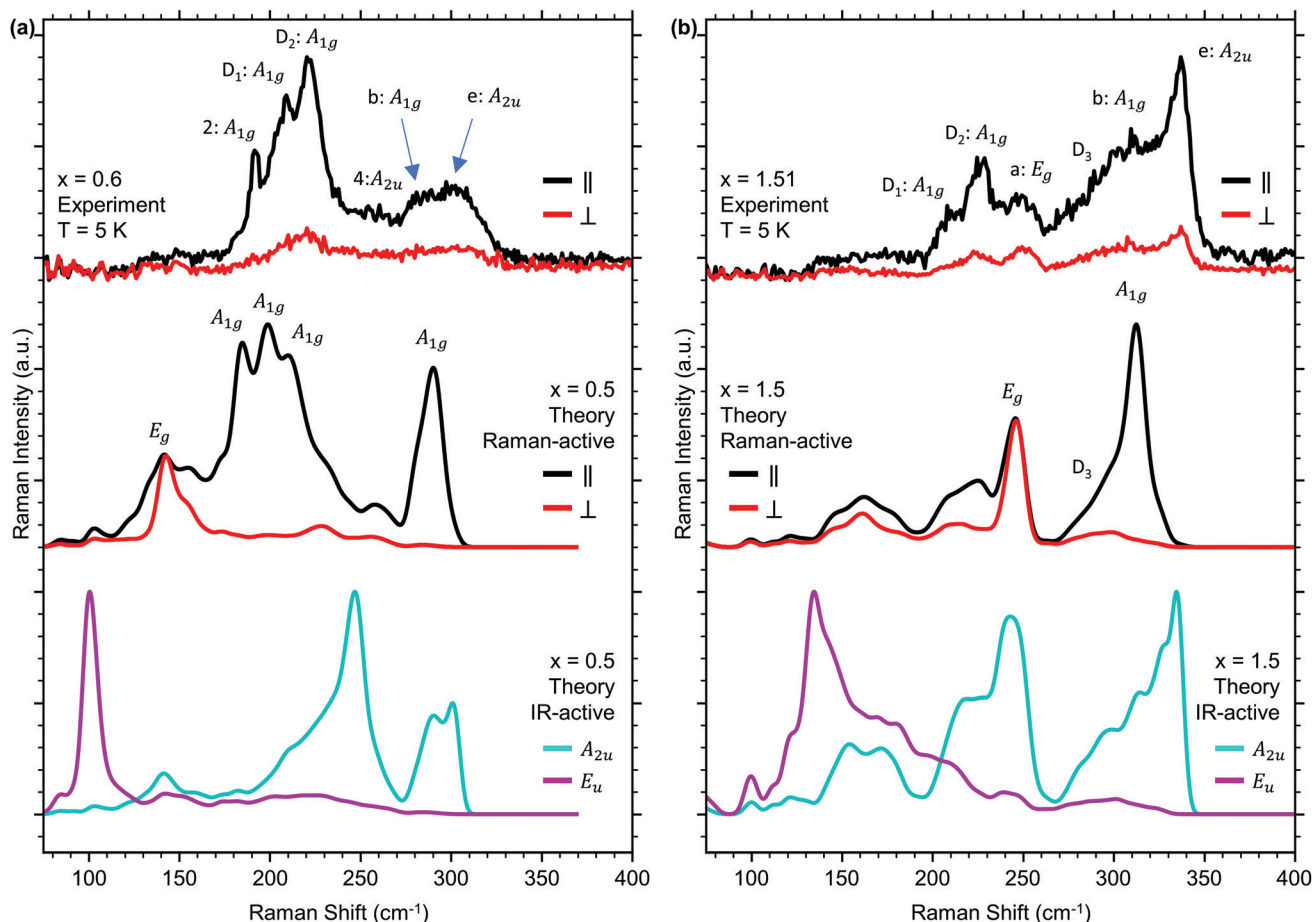


Fig. 4 Assigning the  $\text{ZrS}_x\text{Se}_{2-x}$  Raman mode symmetries for compositions (a)  $x = 0.6$  and (b)  $x = 1.51$  alloys. Experimental polarization-resolved Raman measurements (top curves) are compared to simulated polarized Raman (center curves) and IR spectra (bottom curves), which are all offset vertically for clarity. In the experimental and theoretical polarized Raman spectra, the black curves represent measurements where the excitation laser is co-polarized ( $\parallel$ ) with the collection polarizer, whereas the red curves represent measurements where the excitation laser is cross-polarized ( $\perp$ ) with the collection polarizer. The theoretical IR spectra show vibrations from  $A_{2u}$  modes (cyan curves) and  $E_u$  modes (magenta curves) that are both normalized by the peak of greatest intensity. Certain features are labeled with either the numbers and letters used in Fig. 3a and b or vibrational symmetries where relevant. Experimental spectra are taken at 5 K with 532 nm excitation.

of these features with the alloy broadened primary peaks.<sup>53</sup> The  $\text{ZrS}_2$  overtone modes in the  $600\text{--}700\text{ cm}^{-1}$  range (upside-down magenta triangles of Fig. 3b) persist in the S-rich alloys as  $x$  is decreased from 2 to 1.14 and shift to lower frequencies. There is a very weak presence of these features in the  $x = 1.05$  sample, but they are no longer present as  $x$  is further decreased.

An interesting observation of the  $\text{ZrS}_x\text{Se}_{2-x}$  Raman spectra is the alloy-induced activation and enhancement of new features (blue diamonds in Fig. 3b). We refer to these as disorder modes and label them as  $D_n$  ( $n = 1, 2, 3$ ). Peaks  $D_1$  and  $D_2$  appear at  $202\text{ cm}^{-1}$  and  $219\text{ cm}^{-1}$ , respectively, when  $x$  is increased from 0 to 0.15. Polarization-resolved Raman measurements of the  $x = 0.6$  sample in the top curves of Fig. 4a confirm these features as having  $A_{1g}$  symmetry since they are present in the  $\parallel$  configuration and not the  $\perp$  configuration. It is possible that the origin of  $D_2$  may be related to alloy disorder-induced enhancement<sup>57</sup> of the  $A_{2u}$  peak 3 in  $\text{ZrSe}_2$  (see Fig. 3b) since our theoretical IR spectra in the bottom curves of Fig. 4a show a pronounced  $A_{2u}$  mode at  $\approx 246\text{ cm}^{-1}$ . However, our theoretical

Raman spectra (middle curves of Fig. 4a) predict three features with  $A_{1g}$  symmetry in the relevant frequency range and so we rule out peak 3 from  $\text{ZrSe}_2$  as the origin to peak  $D_2$ . Close inspection of Fig. 3a shows that  $D_1$  and  $D_2$  increase in intensity when  $x$  is increased above 0.15 so that  $D_1$  becomes the dominant feature in the  $x = 0.3$  alloy and  $D_2$  becomes the dominant feature for  $0.6 \leq x \leq 1.14$ . This behavior is reminiscent of results seen in a previous study of  $\text{MoS}_x\text{Se}_{2-x}$  alloys<sup>58</sup> as well as in our recent work on  $\text{WSe}_{2(1-x)}\text{Te}_{2x}$ .<sup>59</sup> In the context of the  $\text{MoS}_x\text{Se}_{2-x}$  alloys, the authors observed the splitting of the  $\text{MoSe}_2$   $A_{1g}$  mode as the material is doped with S atoms.<sup>58</sup> They attribute this behavior to different configurations of S and Se atoms around the Mo atom, which introduces a spatial variance of force constants. This creates a dipole of the alloy unit cell that introduces new vibrations and vibrational phase shifts between adjacent layers that results in splitting of the primary vibrational modes and activation of new modes. Therefore, we assign peaks  $D_1$  and  $D_2$  to originating from different configurations of S and Se atoms around the Zr atom.



The disorder feature D<sub>3</sub> in Fig. 3b manifests as an asymmetrical tail at lower frequencies to the primary A<sub>1g</sub> peak b in ZrS<sub>2</sub> (see top curves of Fig. 4b and the ESI,† Fig. S4). Our theoretical polarization-resolved Raman spectrum of  $x = 1.5$  in Fig. 4b (middle curve, black) shows an asymmetrical tail on the lower frequency side of the primary A<sub>1g</sub> mode, and our simulated spectra in the ESI,† Fig. S7, show that this behavior becomes more prominent as  $x$  is further decreased from 2. As a result, we suggest that this feature results from activation of finite momentum phonons due to alloy disorder.<sup>60,61</sup> Substitutional atoms introduced into the lattice during the alloying process act as scattering centers that break translational symmetry and result in phonon confinement.<sup>62</sup> This causes breakdown of the  $\vec{q} = 0$  Raman selection rule, which allows for activation of finite momentum phonons. Our assignment agrees with the ZrS<sub>2</sub> phonon band calculations of Fig. 3c that show dispersion of the A<sub>1g</sub> band to lower frequencies for finite momentum.

An interesting feature in the alloys that we now comment on is peak e. As discussed previously, we assign the origin of this feature in pure ZrS<sub>2</sub> to an IR-active A<sub>2u</sub>(LO) mode. When ZrS<sub>2</sub> is doped with Se atoms, for example from  $x = 2$  to  $x = 1.8$ , this feature becomes more easily resolvable. Peak e then becomes the most dominant feature as  $x$  is further decreased to 1.51 (see Fig. 3a and polarization-resolved Raman measurements in the top black curve of Fig. 4b). We calculate the theoretical IR spectra for an  $x = 1.5$  sample in the bottom curves of Fig. 4b, which show a prominent A<sub>2u</sub> mode that matches the frequency of peak e in our Raman experiments and supports assignment of this feature to A<sub>2u</sub> symmetry. Revisiting Fig. 3a, we find that further incorporation of Se into the lattice so that  $x$  is decreased below 1.51 then causes the intensity of peak e to decrease. We suggest that the remarkable dominance of IR modes in a Raman spectrum may be due to mixing driven by the random distribution of Zr–S and Zr–Se bonds, which have different ionicity. The loss of translational symmetry by the random distribution of dopant atoms may also relax Raman selection rules and enhance IR modes.<sup>63</sup>

### 3.3 Excitons

SE is performed on bulk crystals at room temperature to measure the real ( $n$ ) and imaginary ( $k$ ) components of the refractive index. TMDs are optically dense and highly birefringent. As a result, measurements on the exposed basal plane, such as those reported here, are sensitive to the ordinary but not the extraordinary refractive index.<sup>64</sup> In Fig. 5a and b, we present measurements of  $n$  and  $k$  for samples across the ZrS <sub>$x$</sub> Se<sub>2– $x$</sub>  alloy series determined by SE, which are taken within 10 minutes of exfoliation to expose a fresh surface and minimize the effects from oxidation. We also account for the presence of any new oxide formation on the exposed crystal face as we have done in ref. 64 (see *Experimental and theoretical methods* section for more details on SE measurements). The data here have been offset vertically for clarity (see the ESI,† Fig. S8, for un-shifted data). Spectral peaks are easily identifiable across the whole alloy series and are fit with Voigt profiles as seen in the example fits in Fig. 5a and b. We extract the energies for peaks in  $k$  from the Voigt fitting and plot them

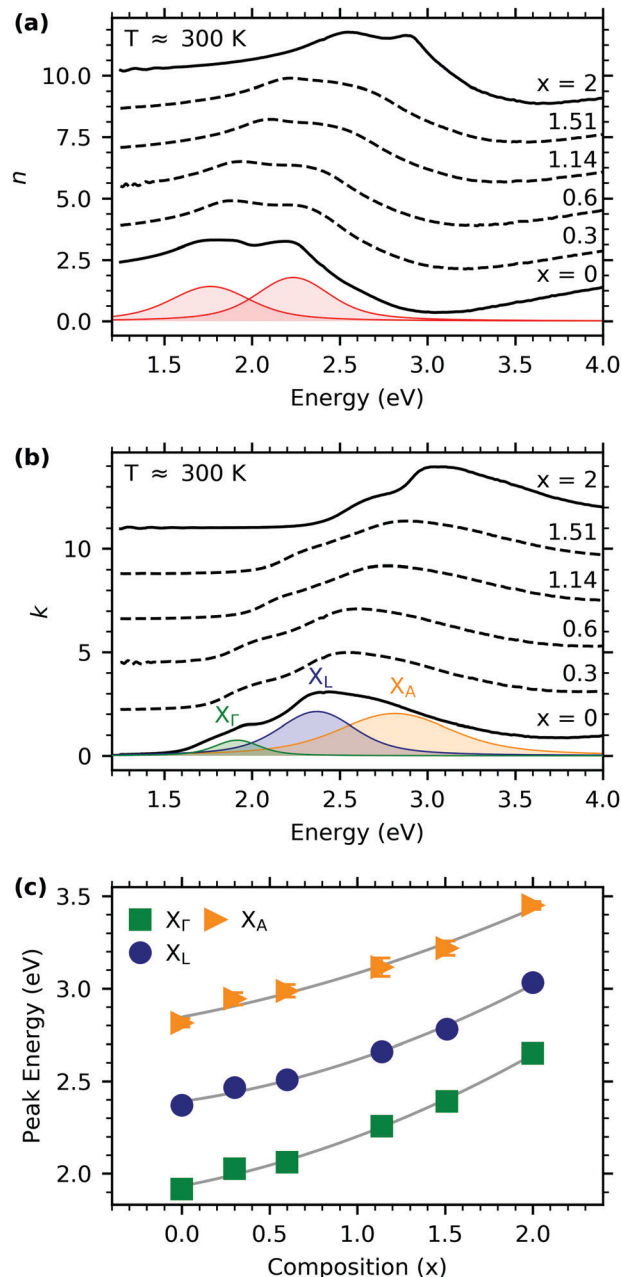


Fig. 5 Optical constants measured by spectroscopic ellipsometry (SE) of ZrS <sub>$x$</sub> Se<sub>2– $x$</sub>  alloys at room temperature. (a) Real ( $n$ ) and (b) imaginary ( $k$ ) components of the complex refractive index. The spectra in panels (a) and (b) are shifted vertically to easily visualize the peak positions. Un-shifted spectra can be found in the ESI,† Fig. S8. The data are best fit with Voigt functions as shown in panels (a) and (b) for ZrSe<sub>2</sub> ( $x = 0$ ). (c) Energies of peaks in  $k$  extracted from Voigt fitting of the data in panel (b). The grey lines are fits to eqn (2). See the ESI,† Fig. S9, for the energies extracted from the peaks in  $n$ .

against alloy composition in Fig. 5c. See the ESI,† Fig. S9, for the energies extracted for peaks in  $n$ .

ZrS <sub>$x$</sub> Se<sub>2– $x$</sub>  are indirect band gap semiconductors. The lowest-energy, direct, allowed optical band gap is at the  $\Gamma$  point with energy between 2.16 eV for ZrSe<sub>2</sub> and 2.81 eV for ZrS<sub>2</sub> as calculated at the GW0 level of theory (see *Experimental and theoretical methods* section), which are slightly higher than

previous GW0 calculations.<sup>65</sup> For the electronic band structures of ZrSe<sub>2</sub> and ZrS<sub>2</sub>, see the ESI,† Fig. S10. The lowest energy peak labeled X<sub>G</sub> that is observed in Fig. 5b is likely to be the  $\Gamma$ -point exciton as suggested previously.<sup>66</sup> Comparing this peak position extracted from Voigt fitting ( $1.92 \pm 0.01$  eV for ZrSe<sub>2</sub> and  $2.65 \pm 0.01$  eV for ZrS<sub>2</sub>) to the calculated  $\Gamma$ -point direct band gap, we estimate that the exciton binding energy is in the range of  $\approx 200$  meV for both ZrSe<sub>2</sub> and ZrS<sub>2</sub>. We hesitate to report on the alloy dependence of this value since it is highly dependent on the GW0 excited-state calculations that are known to have sizable uncertainty. Our estimate for the  $\Gamma$ -point exciton binding energy for ZrSe<sub>2</sub> and ZrS<sub>2</sub> carries the same uncertainty as the single-particle band gap values calculated at the GW0 level of theory. The peaks labeled X<sub>L</sub> and X<sub>A</sub> in the SE spectra of Fig. 5b may originate from direct transitions at the L and A points, which agree with assignments made in ref. 66 since our SE technique is sensitive only to the refractive index with the electric field in the basal plane.

The energies of peaks X<sub>G</sub>, X<sub>L</sub>, and X<sub>A</sub> obtained by fitting three Voigt peaks to the data corresponding to  $k$  are plotted in Fig. 5c as a function of alloy composition, and we find that they all blue-shift continuously with increasing S concentration (increasing  $x$ ) and display moderate bowing. Therefore, we fit these peak energies as a function of alloy composition to a band bowing equation of the form

$$E(x) = \frac{x}{2}E(\text{ZrS}_2) + \left(1 - \frac{x}{2}\right)E(\text{ZrSe}_2) - b\frac{x}{2}\left(1 - \frac{x}{2}\right) \quad (2)$$

where  $E(x)$  is an excitonic transition energy associated with alloy composition  $x$ ,  $E(\text{ZrS}_2)$  and  $E(\text{ZrSe}_2)$  are the transition energies of the relevant peak in either ZrS<sub>2</sub> or ZrSe<sub>2</sub>, and  $b$  is the band bowing parameter which is used to describe deviation from linearity. Fits of the alloy dependence of peaks X<sub>G</sub>, X<sub>L</sub>, and X<sub>A</sub> are plotted in Fig. 5c as grey lines from which we extract bowing parameters 0.35 eV, 0.36 eV, and 0.22 eV, respectively. These values are much larger than those calculated and observed in similar chalcogen alloys such as WS<sub>2</sub>(1- $x$ )Se<sub>2 $x$</sub>  and MoS<sub>2</sub>(1- $x$ )Se<sub>2 $x$</sub> .<sup>67</sup> Band gap bowing parameters are typically determined by a combination of lattice mismatch as well as a mismatch between the valence band and conduction band offsets of the end compounds. ZrS<sub>2</sub> and ZrSe<sub>2</sub> have similar in-plane lattice constants, but they have a calculated valence band offset of  $\approx 1$  eV, which is much larger than the conduction band offset of  $\approx 0.1$  eV.<sup>68</sup> WS<sub>2</sub>(1- $x$ )Se<sub>2 $x$</sub>  and MoS<sub>2</sub>(1- $x$ )Se<sub>2 $x$</sub> , on the other hand, have similar valence band offsets and conduction band offsets and a similarly small bowing parameter.<sup>67</sup> Therefore, we attribute the bowing parameters observed here to the large valence band offset in ZrS <sub>$x$</sub> Se<sub>2- $x$</sub> .

For NIR refractive applications, such as modulators for integrated photonics, the benefit of strong light-matter interaction (*i.e.*, large  $n$ ) with below-band gap photons is offset by absorption. Here we find that optical loss in the NIR decreases as the band gap increases with S concentration, as expected. For ZrS<sub>2</sub>, we find  $k \approx 0.01$  well below the band gap, which is substantially lower than we found in an earlier study of NIR optical properties of transition metal disulfides. The lower loss

found here is likely due to higher crystal quality. Another contributing factor may be the better control and understanding in this study of the native oxide and its effect on SE.

## 4 Conclusions

We have explored the behavior of phonons and excitons in ZrS <sub>$x$</sub> Se<sub>2- $x$</sub>  by combining Raman spectroscopy and SE. Low-temperature, polarization-resolved Raman measurements of bulk flakes revealed intriguing changes in phonon mode activity with alloying. DFT modeling of the phonon dispersion curves and Raman spectra demonstrated that these observations can be explained by long-range Coulomb interactions arising from the ionic nature of the intralayer chemical bonds. These calculations allowed us to clarify disagreements in the literature surrounding ZrS<sub>2</sub> mode assignments: the primary broad peak in the ZrS<sub>2</sub> Raman spectrum originates from an optical A<sub>1g</sub> phonon and two nearly degenerate IR phonons that become Raman active due to dipolar interactions. We then used the vibrational mode symmetry assignments obtained for the pure compounds to track the evolution of the phonons with alloying. The optical A<sub>1g</sub> and E<sub>g</sub> features displayed two-mode behavior due to their large frequency separation in the parent compounds, and we also discovered activation of new phonons as well as the enhancement of IR modes that are otherwise only weakly active in ZrS<sub>2</sub> and ZrSe<sub>2</sub>. Comparison of Raman measurements for select alloys with simulated IR spectra revealed that some compositions had spectra that were completely dominated by IR phonons, which was attributed to the high ionicity of the intralayer chemical bonds in these materials. Room-temperature SE measurements revealed blue-shifting of the direct, allowed optical transitions with increasing S content. By combining SE data with electronic structure calculations, we obtained a rough estimate for the  $\Gamma$ -point exciton binding energy at room temperature of  $\approx 200$  meV for ZrSe<sub>2</sub> and ZrS<sub>2</sub>. For NIR light below the direct band gap, ZrS <sub>$x$</sub> Se<sub>2- $x$</sub>  materials featured strong light-matter interaction ( $n \gtrsim 2$ ) and rather low optical loss ( $k \lesssim 0.5$ ) that decreased with increasing S content. These optical characteristics, when combined with recent predictions of strain-tunable properties in ZrS<sub>2</sub>,<sup>7-10</sup> suggest ZrS <sub>$x$</sub> Se<sub>2- $x$</sub>  alloys will find applications in atomically-thin, high-performance, and dynamically-tunable photodetectors and photovoltaics operating across visible to IR wavelengths.

## Conflicts of interest

There are no conflicts to declare.

## Acknowledgements

The work was financially supported by the National Science Foundation (NSF) through the Pennsylvania State University 2D Crystal Consortium – Materials Innovation Platform (2DCC-MIP) under NSF cooperative agreement DMR-1539916. P. Vora, S. Oliver, and S. Yee also acknowledge support from the George

Mason University (GMU) Quantum Materials Center, the GMU Presidential Scholars Program, and the GMU Undergraduate Research Scholars Program. H. Komsa and A. Hashemi are grateful to the Academy of Finland for the support under Projects No. 286279 and 311058. H. Komsa and A. Hashemi also thank CSC-IT Center for Science Ltd for generous grants of computer time. R. Jaramillo and A. Singh acknowledge support by an Office of Naval Research MURI through grant #N00014-17-1-2661.

## Notes and references

- 1 K. F. Mak and J. Shan, *Nat. Photonics*, 2016, **10**, 216–226.
- 2 W. Choi, N. Choudhary, G. H. Han, J. Park, D. Akinwande and Y. H. Lee, *Mater. Today*, 2017, **20**, 116–130.
- 3 L. Li, X. Fang, T. Zhai, M. Liao, U. K. Gautam, X. Wu, Y. Koide, Y. Bando and D. Golberg, *Adv. Mater.*, 2010, **22**, 4151–4156.
- 4 L. Li, H. Wang, X. Fang, T. Zhai, Y. Bando and D. Golberg, *Energy Environ. Sci.*, 2011, **4**, 2586.
- 5 M. Mattinen, G. Popov, M. Vehkamäki, P. J. King, K. Mizohata, P. Jalkanen, J. Räisänen, M. Leskelä and M. Ritala, *Chem. Mater.*, 2019, **31**, 5713–5724.
- 6 M. Moustafa, T. Zandt, C. Janowitz and R. Manzke, *Phys. Rev. B: Condens. Matter Mater. Phys.*, 2009, **80**, 035206.
- 7 Y. Li, J. Kang and J. Li, *RSC Adv.*, 2014, **4**, 7396.
- 8 A. Kumar, H. He, R. Pandey, P. K. Ahluwalia and K. Tankeshwar, *AIP Conf. Proc.*, 2015, 090016.
- 9 H. Y. Lv, W. J. Lu, D. F. Shao, H. Y. Lu and Y. P. Sun, *J. Mater. Chem. C*, 2016, **4**, 4538–4545.
- 10 Q. Xin, X. Zhao, X. Ma, N. Wu, X. Liu and S. Wei, *Phys. E*, 2017, **93**, 87–91.
- 11 S. Adachi, *Properties of Semiconductor Alloys*, John Wiley & Sons, Ltd, Chichester, UK, 2009.
- 12 L. M. Xie, *Nanoscale*, 2015, **7**, 18392–18401.
- 13 X. T. Wang, L. Huang, X. W. Jiang, Y. Li, Z. M. Wei and J. B. Li, *J. Mater. Chem. C*, 2016, **4**, 3143–3148.
- 14 M. J. Mleczko, C. Zhang, H. R. Lee, H.-H. Kuo, B. Magyari-Köpe, R. G. Moore, Z.-X. Shen, I. R. Fisher, Y. Nishi and E. Pop, *Sci. Adv.*, 2017, **3**, e1700481.
- 15 H. L. Zhuang and R. G. Hennig, *J. Phys. Chem. C*, 2013, **117**, 20440–20445.
- 16 H. Li, H. Liu, L. Zhou, X. Wu, Y. Pan, W. Ji, B. Zheng, Q. Zhang, X. Zhuang, X. Zhu, X. Wang, X. Duan and A. Pan, *ACS Nano*, 2018, **12**, 4853–4860.
- 17 S. G. Patel, S. K. Arora and M. K. Agarwal, *Bull. Mater. Sci.*, 1998, **21**, 297–301.
- 18 C. R. Whitehouse, H. P. B. Rimmington and A. A. Balchin, *Phys. Status Solidi*, 1973, **18**, 623–631.
- 19 K. Bartwal and O. Srivastava, *Mater. Sci. Eng., B*, 1995, **33**, 115–121.
- 20 A. Ghafari, A. Boochani, C. Janowitz and R. Manzke, *Phys. Rev. B: Condens. Matter Mater. Phys.*, 2011, **84**, 125205.
- 21 A. Ghafari, C. Janowitz and R. Manzke, *J. Phys.: Condens. Matter*, 2013, **25**, 315502.
- 22 A. Ghafari and C. Janowitz, *Comput. Mater. Sci.*, 2019, **169**, 109109.
- 23 M. Moustafa, A. Ghafari, A. Paulheim, C. Janowitz and R. Manzke, *J. Electron Spectrosc. Relat. Phenom.*, 2013, **189**, 35–39.
- 24 M. Moustafa, A. Paulheim, M. Mohamed, C. Janowitz and R. Manzke, *Appl. Surf. Sci.*, 2016, **366**, 397–403.
- 25 M. Moustafa, A. Wasnick, C. Janowitz and R. Manzke, *Phys. Rev. B*, 2017, **95**, 245207.
- 26 A. Hashemi, A. V. Krasheninnikov, M. Puska and H.-P. Komsa, *Phys. Rev. Mater.*, 2019, **3**, 023806.
- 27 F. H. L. Koppens, T. Mueller, P. Avouris, A. C. Ferrari, M. S. Vitiello and M. Polini, *Nat. Nanotechnol.*, 2014, **9**, 780–793.
- 28 G. Kresse and J. Hafner, *Phys. Rev. B: Condens. Matter Mater. Phys.*, 1993, **47**, 558.
- 29 G. Kresse and J. Furthmüller, *Comput. Mater. Sci.*, 1996, **6**, 15.
- 30 I. Hamada, *Phys. Rev. B: Condens. Matter Mater. Phys.*, 2014, **89**, 121103.
- 31 T. Björkman, *J. Chem. Phys.*, 2014, **141**, 074708.
- 32 J. P. Perdew, K. Burke and M. Ernzerhof, *Phys. Rev. Lett.*, 1996, **77**, 3865.
- 33 J. Heyd, G. E. Scuseria and M. Ernzerhof, *J. Chem. Phys.*, 2003, **118**, 8207.
- 34 J. Heyd, G. E. Scuseria and M. Ernzerhof, *J. Chem. Phys.*, 2006, **124**, 219906.
- 35 J. C. V. Klimeš, M. Kaltak and G. Kresse, *Phys. Rev. B: Condens. Matter Mater. Phys.*, 2014, **90**, 075125.
- 36 A. van de Walle and G. Ceder, *J. Phase Equilib.*, 2002, **23**, 348–359.
- 37 A. van de Walle, M. Asta and G. Ceder, *CALPHAD: Comput. Coupling Phase Diagrams Thermochem.*, 2002, **26**, 539–553.
- 38 A. van de Walle, P. Tiwary, M. de Jong, D. Olmsted, M. Asta, A. Dick, D. Shin, Y. Wang, L.-Q. Chen and Z.-K. Liu, *CALPHAD: Comput. Coupling Phase Diagrams Thermochem.*, 2013, **42**, 13–18.
- 39 A. Togo and I. Tanaka, *Scr. Mater.*, 2015, **108**, 1–5.
- 40 T. V. Vu, H. D. Tong, D. P. Tran, N. T. T. Binh, C. V. Nguyen, H. V. Phuc, H. M. Do and N. N. Hieu, *RSC Adv.*, 2019, **9**, 41058–41065.
- 41 S.-D. Guo, Y.-F. Li and X.-S. Guo, *Comput. Mater. Sci.*, 2019, **161**, 16–23.
- 42 N. Glebko, I. Aleksandrova, G. C. Tewari, T. S. Tripathi, M. Karppinen and A. J. Karttunen, *J. Phys. Chem. C*, 2018, **122**, 26835–26844.
- 43 T. Iwasaki, N. Kuroda and Y. Nishina, *J. Phys. Soc. Jpn.*, 1982, **51**, 2233–2240.
- 44 L. Roubi and C. Carlone, *Phys. Rev. B: Condens. Matter Mater. Phys.*, 1988, **37**, 6808–6812.
- 45 S. Mañas-Valero, V. García-López, A. Cantarero and M. Galbiati, *Appl. Sci.*, 2016, **6**, 264.
- 46 S.-i. Uchida and S. Tanaka, *J. Phys. Soc. Jpn.*, 1978, **45**, 153–161.
- 47 G. Lucovsky, R. M. White, J. A. Benda and J. F. Revelli, *Phys. Rev. B: Solid State*, 1973, **7**, 3859–3870.
- 48 K. Nikonov, N. Ehlen, B. Senkovskiy, N. Saigal, A. Fedorov, A. Nefedov, C. Wöll, G. Di Santo, L. Petaccia and A. Grüneis, *Dalton Trans.*, 2018, **47**, 2986–2991.

- 49 I. Chang and S. Mitra, *Adv. Phys.*, 1971, **20**, 359–404.
- 50 D. Wang, X. Zhang, G. Guo, S. Gao, X. Li, J. Meng, Z. Yin, H. Liu, M. Gao, L. Cheng, J. You and R. Wang, *Adv. Mater.*, 2018, **30**, 1803285.
- 51 V. G. Hadjiev, D. De, H. B. Peng, J. Manongdo and A. M. Guloy, *Phys. Rev. B: Condens. Matter Mater. Phys.*, 2013, **87**, 104302.
- 52 M. Zhang, J. Wu, Y. Zhu, D. O. Dumcenco, J. Hong, N. Mao, S. Deng, Y. Chen, Y. Yang, C. Jin, S. H. Chaki, Y.-S. Huang, J. Zhang and L. Xie, *ACS Nano*, 2014, **8**, 7130–7137.
- 53 Y. Chen, D. O. Dumcenco, Y. Zhu, X. Zhang, N. Mao, Q. Feng, M. Zhang, J. Zhang, P.-H. Tan, Y.-S. Huang and L. Xie, *Nanoscale*, 2014, **6**, 2833.
- 54 G. P. Srivastava, *The Physics of Phonons*, Routledge, New York, 1st edn, 1990.
- 55 L. Genzel, T. P. Martin and C. H. Perry, *Phys. Status Solidi*, 1974, **62**, 83–92.
- 56 I. F. Chang and S. S. Mitra, *Phys. Rev.*, 1968, **172**, 924–933.
- 57 S. M. Oliver, R. Beams, S. Krylyuk, I. Kalish, A. K. Singh, A. Bruma, F. Tavazza, J. Joshi, I. R. Stone, S. J. Stranick, A. V. Davydov and P. M. Vora, *2D Mater.*, 2017, **4**, 045008.
- 58 J. Jadcak, D. O. Dumcenco, Y. S. Huang, Y. C. Lin, K. Suenaga, P. H. Wu, H. P. Hsu and K. K. Tiong, *J. Appl. Phys.*, 2014, **116**, 193505.
- 59 S. M. Oliver, J. Young, S. Krylyuk, T. L. Reinecke, A. V. Davydov and P. M. Vora, *Commun. Phys.*, 2020, **3**, 10.
- 60 S. Mignuzzi, A. J. Pollard, N. Bonini, B. Brennan, I. S. Gilmore, M. A. Pimenta, D. Richards and D. Roy, *Phys. Rev. B: Condens. Matter Mater. Phys.*, 2015, **91**, 195411.
- 61 P. Parayanthal and F. H. Pollak, *Phys. Rev. Lett.*, 1984, **52**, 1822–1825.
- 62 X. Zhang, X.-F. Qiao, W. Shi, J.-B. Wu, D.-S. Jiang and P.-H. Tan, *Chem. Soc. Rev.*, 2015, **44**, 2757–2785.
- 63 D. O. Dumcenco, K. Y. Chen, Y. P. Wang, Y. S. Huang and K. K. Tiong, *J. Alloys Compd.*, 2010, **506**, 940–943.
- 64 A. Singh, Y. Li, B. Fodor, L. Makai, J. Zhou, H. Xu, A. Akey, J. Li and R. Jaramillo, *Appl. Phys. Lett.*, 2019, **115**, 161902.
- 65 M. Abdulsalam and D. P. Joubert, *Phys. Status Solidi*, 2016, **253**, 705–711.
- 66 S. C. Bayliss and W. Y. Liang, *J. Phys. C: Solid State Phys.*, 1982, **15**, 1283–1296.
- 67 J. Kang, S. Tongay, J. Li and J. Wu, *J. Appl. Phys.*, 2013, **113**, 143703.
- 68 C. Zhang, C. Gong, Y. Nie, K.-a. Min, C. Liang, Y. J. Oh, H. Zhang, W. Wang, S. Hong, L. Colombo, R. M. Wallace and K. Cho, *2D Mater.*, 2016, **4**, 015026.